Research Square

Preprints are preliminary reports that have not undergone peer review.
They should not be considered conclusive, used to inform clinical practice,
or referenced by the media as validated information.

From Hyperspectral Signatures to Robotic LiDAR-Based Moisture Monitoring: A Machine Learning-Based Framework

Parham Jafary
Toronto Metropolitan University
Kourosh Zareinia
Toronto Metropolitan University
Lesley G. Campbell
Toronto Metropolitan University
Habiba Bougherara
habiba.bougherara@torontomu.ca

Toronto Metropolitan University

Research Article

Keywords: Hyperspectral spectroscopy, Machine learning, Intelligent water detection, Soilless Media, Controlled Environment Agriculture

Posted Date: August 27th, 2026

DOI: https://doi.org/10.21203/rs.3.rs-10712205/v1

License: This work is licensed under a Creative Commons Attribution 4.0 International License.
Read Full License

Additional Declarations: No competing interests reported.

From Hyperspectral Signatures to Robotic LiDAR-Based Moisture Monitoring: A Machine Learning-Based Framework

Parham Jafary[1], Kourosh Zareinia[1], Lesley G. Campbell[2], Habiba Bougherara[1*]

[1]Dept. Of Mechanical, Industrial, and Mechatronics Eng., Toronto Metropolitan University, Toronto, Ontario, Canada

[2]Dept. Of Chemistry and Biology, Toronto Metropolitan University, Toronto, Ontario, Canada

[*]Corresponding Author: habiba.bougherara@torontomu.ca

Abstract

Early, non-invasive detection of moisture deficits in soilless substrates is essential for precision irrigation and condition monitoring in controlled-environment agriculture. However, widely used substrates such as rockwool remain under-characterized spectrally, while existing sensing approaches are often contact-based or limited to laboratory conditions. This study presents a laboratory-to-robotic-deployment framework for non-contact estimation of volumetric water content (VWC) in horticultural rockwool. High-resolution UV–Vis–NIR spectroscopy spanning 200–2500 nm was first used to characterize moisture-dependent reflectance across eleven VWC levels. A one-dimensional convolutional neural network (1D-CNN) was developed for full-spectrum classification. A material-optimized rockwool water index (RWI) was then derived by identifying the wavelength triplet that maximized classification performance. Further, a multi-learner spectral drought (MLSD) model was developed and optimized for reduced-feature classification, improving the baseline class-average F1-score by 15.9% and achieving precision above 97% for nine VWC levels. Finally, the laboratory findings were translated into a practical sensing experiment using a LiDAR mounted on a robotic platform. Visible imagery, active near-infrared return, depth, and signal-quality measurements were acquired from full-size rockwool cubes under variations in moisture content, sensor distance, and ambient illumination. Gravimetric measurements provided reference VWC, while validation was performed by holding out complete cubes and acquisition sessions. The multimodal model achieved an average precision of 92.9% across VWC classes. These results connect laboratory spectral characterization with deployable active optical sensing, demonstrating a practical framework toward non-contact robotic root-zone monitoring and automated irrigation.

Keywords: Hyperspectral spectroscopy, Machine learning, Intelligent water detection, Soilless Media, Controlled Environment Agriculture.

Nomenclature

Abbreviation	Definition
VWC	Volumetric Water Content (%)
UV–Vis–NIR	Ultraviolet–Visible–Near Infrared
HSI	Hyperspectral Imaging
RH	Relative Humidity
NMDI	Normalized Multi-band Drought Index
RWI	Rockwool Water Index
PLS-DA	Partial Least Squares Discriminant Analysis
SIMCA	Soft Independent Modelling of Class Analogy
SVM	Support Vector Machine
RF	Random Forest
KNN	k-Nearest Neighbours
ANN	Artificial Neural Network
MLSD	Proposed Multi-Learner Spectral Drought model
1D-CNN	Proposed One-Dimensional Convolutional Neural Network
P, R, F1	Precision, Recall, and F1-score metrics

1 Introduction

Controlled-environment agriculture and soilless cultivation enable precise regulation of crop water and nutrient supply, supporting higher resource-use efficiency and more consistent production than conventional cultivation systems. However, these benefits depend on maintaining extensive condition monitoring, especially moisture conditions within the root-zone as water stress affects plants growth and yield substantially [1]. To prevent the associated labor costs of such measures offset productivity, automation using robotic and intelligent monitoring systems is essential. In recent years, artificial intelligence has been used for pest detection [2] and growth monitoring [3], autonomous vehicles have been developed for agricultural use [4], and automated precise harvesting tools have been developed for delicate fruits [5]. Nonetheless, root-zone moisture-monitoring studies have focused mostly on soil [6, 7], relied on expensive multi-sensor systems [8], or been limited to contact measurements using dielectric or inserted sensors [9, 10]. While these techniques can be effective for point measurement and lab-scale process control, the associated cost of installing physical sensors and the maintenance complexity make them impractical for large scale root-zone monitoring, outlining a clear gap for non-invasive and cost-effective moisture monitoring systems for soilless media.

Rockwool (stone wool) is extensively used in commercial soilless production because of its high porosity, water-holding capacity, structural stability, and aeration in the root zone without the biological variability associated with soil [11]. However, despite its widespread use in hydroponic production, the spectral behavior of rockwool across varying moisture levels remains poorly characterized, making accurate monitoring of its moisture state challenging. Embedded sensors based on capacitance, frequency-domain reflectometry, electrical conductivity, or matric potential can provide continuous measurements [10, 12]. However, their outputs may depend on sensor placement, substrate density, root development, salinity, temperature, and substrate-specific calibration. For example, plant-root development has been shown to affect frequency-domain reflectometry calibration [13].

Alternatively, hyperspectral imaging (HIS) is a widely used non-destructive sensing technique in agriculture [14] applied to a variety of applications such as plant metabolic response detections [15], leaf water content assessment [16], and crop quality classification [17]. Optical sensing provides an alternative means of estimating moisture without inserting a sensor into the root zone. The physical basis of this approach is the influence of water on absorption, scattering, and surface reflectance. In earlier research, Wang and Qu demonstrated that adding water to soil alters absorption in the NIR and shortwave infrared (SWIR) spectral regions [18], showing that increasing moisture typically reduces reflectance in these regions. They proposed normalized multi-band drought index (NMDI) for monitoring soil and vegetation moisture conditions. NMDI combines reflectance from one NIR band (860 nm) and two SWIR bands (1640 nm and 2130 nm) to enhance sensitivity to water content. More recent approaches have combined hyperspectral information and machine learning to account for nonlinear relationships between moisture and reflectance to estimate soil moisture content [19]. However, most existing investigations have focused on mineral soils, vegetation, or plant water status. Comparatively little attention has been given to the spectral response of horticultural rockwool across systematically controlled volumetric water content (VWC) levels. Ergo, the subtle reflectance changes associated with VWC levels may not be optimally captured by the original NMDI formulation. A material-specific wavelength-selection procedure is therefore needed to identify a compact spectral representation of rockwool moisture.

Although laboratory spectrometers are useful for identifying moisture-sensitive wavelengths, their cost, size, and controlled measurement conditions limit practical deployment in commercial cultivation, creating a gap between laboratory spectral discovery and field sensing. Active optical sensing offers a way to bridge this gap: LiDAR and time-of-flight cameras provide depth and near-infrared intensity under variable conditions, and when combined with RGB and auxiliary metadata, may capture moisture information in a multimodal form. In addition, LiDAR has become one of the most widely adopted sensing modalities in robotics due to its robustness, real-time 3D perception capability, and decreasing cost [20], with extensive use in mapping [21], autonomous navigation [22], manipulation [23], and agricultural robotics systems as demonstrated in recent studies [24–26]. This widespread adoption makes it a particularly interesting candidate for translation from laboratory sensing concepts to deployable agricultural monitoring systems. However, LiDAR intensity is affected by distance, angle, and system properties [27, 28],

requiring correction before moisture interpretation. In robotics, this enables non-contact monitoring of multiple rockwool cubes, moving beyond probe-based RGB-D approaches [29], and testing whether moisture-related optical and geometric signals can be recovered in practical deployment settings.

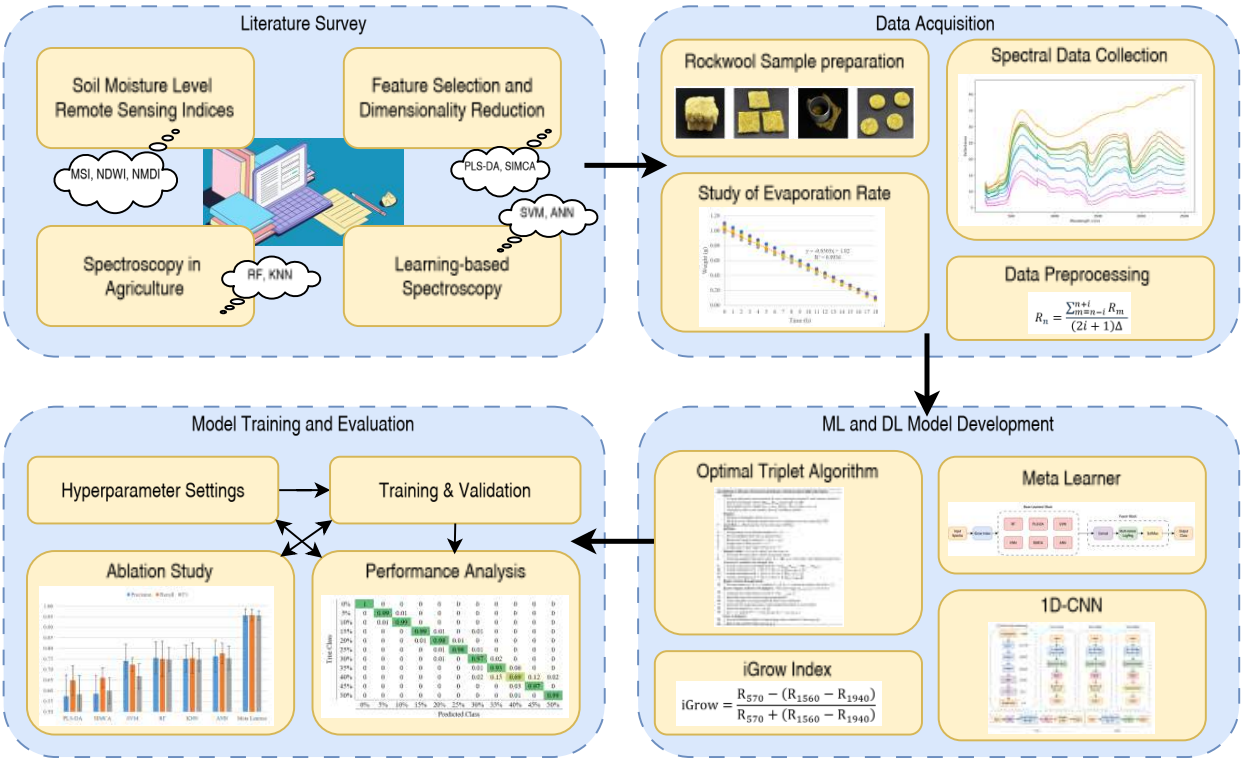


Fig. 1 – Overall workflow of finding the optimal prediction model for rockwool VWC classification in the study.

To address these research gaps, this study presents a laboratory-to-robotic-deployment framework for non-contact VWC monitoring in horticultural rockwool. High-resolution UV–Vis–NIR spectroscopy is first used to characterize moisture-dependent reflectance across eleven VWC levels. A wavelength-optimization procedure is used to derive a material-specific rockwool water index (RWI). Machine learning models are then developed and optimized for VWC classification using full-spectrum and reduced features. Finally, the laboratory investigation is extended to full-size rockwool cubes using a robot-mounted LiDAR system. The overall workflow of the research is illustrated in Fig. 1 and the principal contributions of this study are:

- A high-resolution characterization of moisture-dependent reflectance in horticultural rockwool across the UV–Vis–NIR spectrum and eleven controlled VWC levels.
- A material-specific wavelength-selection framework and RWI for representing rockwool moisture using a compact set of complementary spectral bands.
- A 1-dimensional convolutional neural network (1D-CNN) for full-spectrum VWC classification and a multi-learner spectral drought model (MLSD) for reduced-feature VWC classification.
- A multimodal, robot-mounted standoff sensing framework for estimating VWC in full-size rockwool cubes using RGB, active-infrared, depth, and LiDAR signal-quality information.
- A deployment-oriented evaluation incorporating changes in sensor distance, viewing geometry, ambient illumination, physical cubes, and acquisition sessions.

Through these contributions, the study connects controlled spectral characterization with practical active sensing. The resulting framework provides a pathway from laboratory-scale identification of moisture-sensitive optical behavior to non-contact robotic root-zone monitoring for automated irrigation in controlled environment agriculture.

2 Materials and Methods

This study employed a two-stage framework comprising laboratory spectral characterization and robotic LiDAR-based moisture sensing. First, spectral data were collected, and machine-learning models were developed to characterize rockwool across eleven VWC levels and identify informative wavelengths. The findings were then extended to full-size rockwool cubes using a robot-mounted LiDAR under varying measurement conditions. The overall workflow is illustrated in Fig. 1, and each stage is detailed in the following sections.

Table 1 – Parameters of the tested samples.

Parameter	Value
Count	114
Diameter (mm)	16.38 ± 0.37
Thickness (mm)	4.87 ± 0.21
Volume (cm^3)	1.03 ± 0.07
Dry Weight (g)	0.09 ± 0.02
Submerged Weight (g)	1.05 ± 0.04

2.1 Spectroscopic Characterization

Spectroscopic characterization was conducted to investigate moisture-dependent changes in rockwool reflectance across the UV–Vis–NIR spectrum. This stage included preparing samples at controlled VWC levels, acquiring their reflectance spectra, and preprocessing the collected data that are described in the subsequent sections.

2.1.1 Sample Preparation

Rockwool cubes (Grodan A-OK 1.5" Starter Plugs, Roermond, Netherlands) were used as experimental material. The spectrophotometer powder cell had an inner diameter of 17 mm and a depth of 5 mm, whereas the rockwool cubes had approximate dimensions of $2.5 \times 2.5 \times 2.5\ cm^3$. Therefore, the rockwool cubes were cut into discs compatible with the sample holder. To do so, a custom tool was designed and fabricated using 3D printing (Fig. 2). The cubes were inserted into the device, secured using a handle, and sliced into 5 mm-thick layers using a utility knife. The target thickness of each sample was 5 mm to match the depth of the spectrophotometer sample holder. A circular punch was then used to cut the layers into 17 mm diameter discs (Fig. 3), resulting in a total of 114 prepared samples. Due to the flexibility and compressibility of the material, the resulting samples exhibited slight dimensional variability (the distribution is presented in Fig. 4). Therefore, each sample was labelled, and its dimensions and mass were recorded to calculate the VWC of each sample (Table 1).

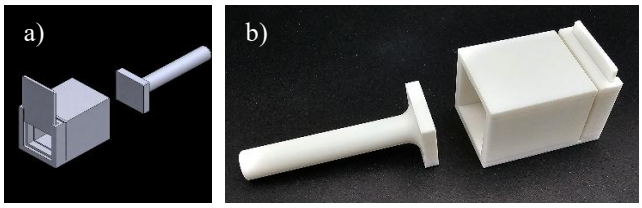


Fig. 2 – Slicing tool for cutting the rockwool cubes, a) The designed parts in SolidWorks environment b) The 3D printed parts used for slicing rockwool cubes.

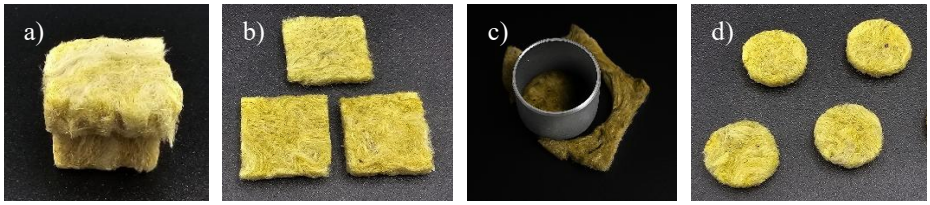


Fig. 3 – Rockwool sample preparation steps a) Initial rockwool cube b) Sliced rockwool plate (average $t = 4.87 \pm 0.21mm$) c) Punching rockwool plate with a 16mm punch d) Final rockwool disc (average $d = 16.38 \pm 0.37mm$)

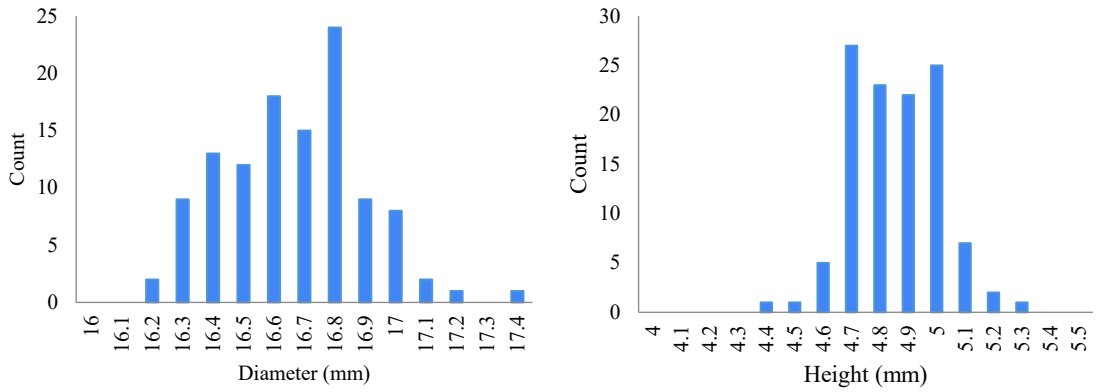


Fig. 4 – Histogram of diameter and thick distribution of rockwool samples.

2.1.2 Experiment Setup

A UV-Vis-NIR spectrophotometer (Cary 5000, Varian Inc., Palo Alto, California, USA) equipped with the UV-Vis-NIR Powder Cell Kit accessory was used to collect spectral data. The instrument was set to measure reflectance (%) of the samples over a wavelength range of 200-2500 nm with a spectral resolution of 1 nm and a scan rate of 1200 nm/min. A white reference baseline measurement was performed for instrument calibration by scanning a polytetrafluoroethylene (PTFE) reference disc. The calibrated reflectance (R) values were calculated using Eq. (1). Each sample spectrum was recorded under identical measurement conditions to ensure consistency across measurements.

$$R_{calibrated} = \frac{R_{measured}}{R_{baseline}} \times 100 \qquad (1)$$



Fig. 5 – a) Cary 5000 machine for UV-Vis-NIR spectroscopy b) Weighing samples before collecting reflectance data c) PTFE control used for establishing baseline (on the left) and sample holder used for each experiment (on the right).

2.1.3 Data Collection

To ensure uniform water distribution within each sample, the samples were first submerged in water and then allowed to dry under natural convection in the laboratory environment. Five samples were submerged and weighed periodically to obtain the evaporation rate (Fig. 6) which served as a guideline for scheduling subsequent spectral measurements. Each sample was submerged into water for 5 seconds to achieve full saturation. The VWC for sample i at time t was calculated by dividing the volume of water within the sample by the total sample volume, using Eq. (2).

$$\theta(i,t) = \left.\frac{V_w}{V_s + V_w}\right|_{i,t} = \left.\frac{m_w}{\alpha m_s + m_w}\right|_{i,t} = \left.\frac{m_i - m_s}{(\alpha - 1)m_s + m_i}\right|_{t} \qquad (2)$$

Where V_w, V_s represent the volumes of water and sample, respectively, m_w, m_s represent the mass of water and the dry mass of the sample, respectively, and $\alpha = \rho_w/\rho_s = 11.44$ represents the ratio of water density to sample density. The sample volume can be calculated by $V_s = (\pi d^2 t)/4$ where d and t represent the sample diameter and thickness,

respectively. The water volume in each sample at the time of spectral measurement was calculated using Eq.(2) based on the measured wet mass of the sample (m_i).

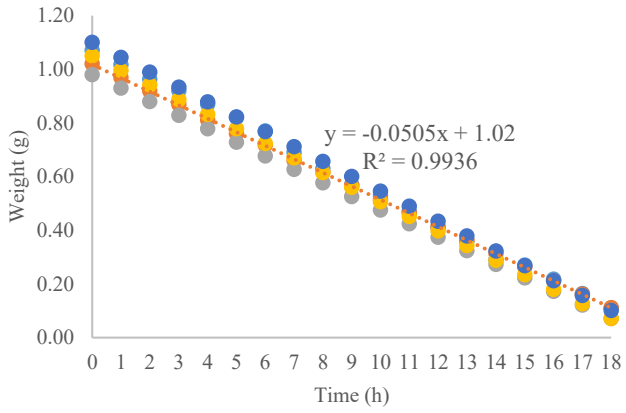


Fig. 6 – Temporal evaporation rate of water content in rockwool samples under natural convection, with RH=52% T=22.1ºC.

It was observed that fully saturated samples exhibited a VWC of approximately $\theta = 50 \pm 3.9\%$ and spectral measurements were therefore collected at approximately 5% increments during the drying process. Therefore, for each VWC level $i \in \{0, 5, \dots, 50\}$ and each sample $j \in [1,100]$ a spectral measurement was recorded, resulting in a total of 1100 spectral measurements each containing 2301 wavelength data points. The data were collected over a period of three months using the experimental setup described in Sec. 2.2 and 2.1. All measurements were conducted under consistent laboratory conditions to minimize environmental variability.

2.1.4 Data Preprocessing

The reflectance readings were smoothed using a moving average filter as defined in Eq.(3), to reduce small fluctuations between successive wavelength measurements.

$$R_n = \frac{\sum_{m=n-i}^{n+i} R_m}{(2i+1)\Delta} \qquad (3)$$

Where R_n is the smoothed reflectance at wavelength n, R_m is the measured reflectance, Δ is the wavelength interval between two consecutive measurements, and i defines the number of neighboring readings included in the averaging window. In this study, these parameters were set to $i = \Delta = 1$. Results from all experiments were preprocessed using this filtering approach and combined to form the final spectral signature library. The processed spectra were then used as input features for subsequent machine learning and deep learning models.

2.2 Full-Spectrum VWC Classification

To exploit the sequential structure of spectral data, a 1-dimensional convolutional neural network (1D-CNN) was developed for end-to-end learning from reflectance spectra. Unlike conventional machine learning models that rely on handcrafted features or predefined spectral indices, the 1D-CNN learns hierarchical feature representations directly from the spectral input, enabling the automatic extraction of local absorption patterns, band interactions, and nonlinear relationships across wavelengths.

2.2.1 1D-CNN Model

In the proposed architecture, the input spectrum $\mathbf{x} \in \mathbb{R}^p$ is represented as a one-dimensional spectral vector and processed through successive one-dimensional convolutional layers that apply learnable filters along the wavelength axis. Each convolution operation is expressed by Eq. (5)

$$h_k(i) = f\left(\sum_{j=1}^{L} w_{k,j}\ x_{i+j-1} + b_k\right) \quad (5)$$

where $h_k(i)$is the output of the k-th filter at position i, $w_{k,j}$and $b_k$denote the convolutional weights and bias, L is the kernel size, and $f(\cdot)$ is a nonlinear activation function. The architecture was designed to progressively extract localized spectral features associated with moisture-dependent absorption patterns.

The proposed 1D-CNN architecture consists of three sequential convolutional blocks (illustrated in Fig. 7). The first block applied 16 filters with a kernel size of 7, followed by batch normalization, a ReLU activation function, and max pooling with a stride (pooling factor) of 2. The second block applied 32 filters with a kernel size of 5 followed by the same normalization, activation, and pooling operations. The third block applied 64 filters with a kernel size of 3, followed by batch normalization and ReLU activation. To obtain a fixed-length feature representation independent of the input spectral resolution, an adaptive average pooling layer was applied, reducing the feature map to a 64-dimensional feature vector. This feature representation =was then passed to a fully connected classifier consisting of one hidden layer with 64 neurons, ReLU activation, and dropout regularization (dropout rate = 0.3), followed by an output layer with Kneurons corresponding to the number of VWC classes.

Model parameters were optimized using the Adam optimizer with a learning rate of 10^{-3} and L2 weight decay of 10^{-4}. The categorical cross-entropy loss function was used for training. The network was trained for 250 epochs with a mini-batch size of 16 samples. By jointly learning hierarchical spectral features and class decision boundaries in an end-to-end manner, the proposed 1D-CNN provided a deep learning framework for modelling nonlinear spectral patterns associated with varying water content levels and complements classical chemometric and machine-learning approaches.

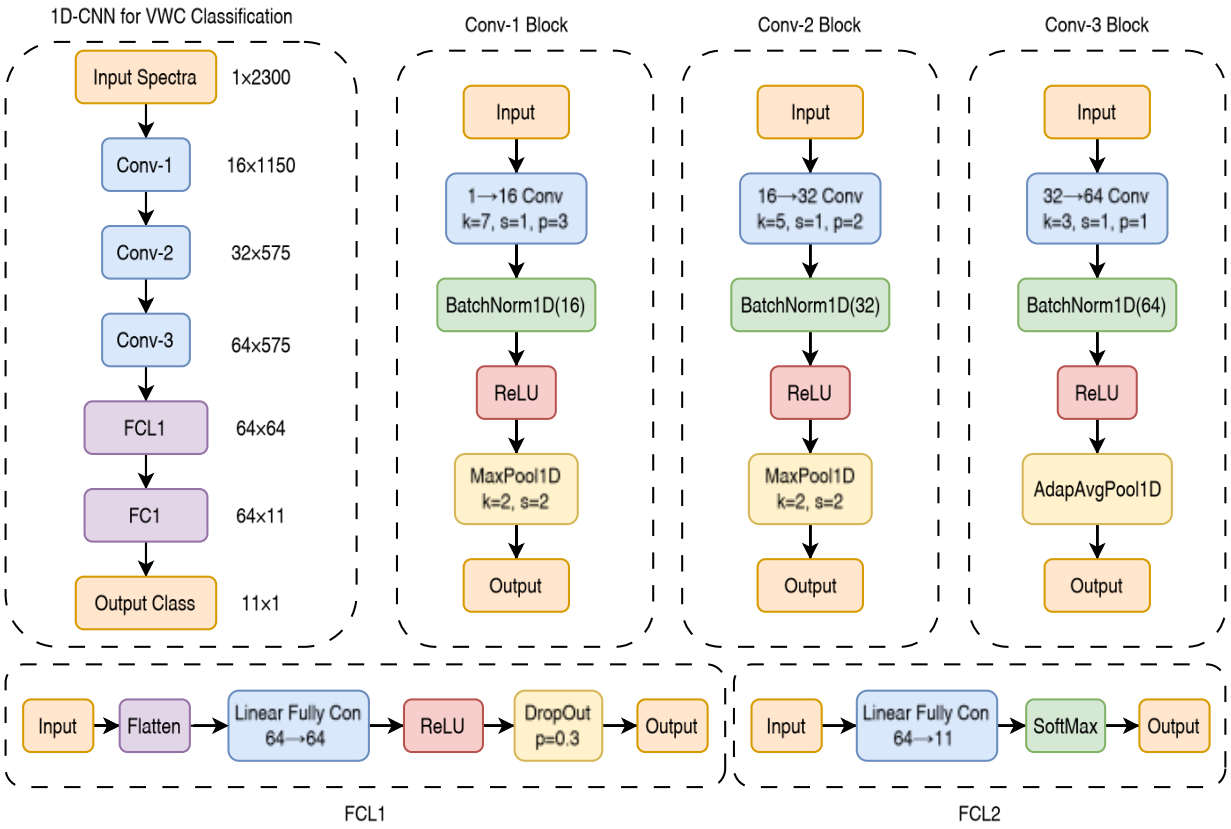


Fig. 7 – Architecture of the proposed one-dimensional convolutional neural network (1D-CNN) for volumetric water content (VWC) classification. The input reflectance spectrum is processed by three sequential convolutional blocks operating along the wavelength axis; the extracted features are then fed to two fully connected layers for classification.

2.3 Rockwool Water Index

Spectral indices are widely used to simplify spectral interpretation and reduce the need to analyze the full wavelength spectrum. Nonetheless, many existing indices were primarily developed for soil [18, 30, 31] and are not ideal for the spectral behavior of rockwool substrates. Therefore, developing a material-specific index for this widely used substrate could enable more reliable discrimination of water content levels. This problem can be formulated as an optimization task to identify an optimal wavelength triplet (λ_a, λ_b, λ_c) through Eq (4) that maximizes the classification performance for VWC. Multiband indices combine reflectance values from selected wavelengths to enhance sensitivity to specific material properties while suppressing background spectral variability.

$$I(\lambda_a, \lambda_b\, \lambda_c) = \frac{R(\lambda_a) - [R(\lambda_b) - R(\lambda_c)]}{R(\lambda_a) + [R(\lambda_b) - R(\lambda_c)]} \quad (4)$$

Given 2301 wavelengths at which reflectance was measured, the number of possible wavelength triplets in the search space (M) can be calculated as $M = 2301 \times 2300 \times 2299 \cong 12.17 \times 10^9$. This highlights the importance of using a systematic search strategy to solve the problem; hence, Algorithm-1 is proposed. This algorithm was first applied using $\delta W = 50$ coupled with a Random Forest classifier to identify wavelength regions that produced the highest classification accuracy. After identifying the promising wavelength ranges for λ_a, λ_b, λ_c, the algorithm was applied again using $\delta W = 10$ to determine the optimal wavelength triplet.

2.4 Reduced-Feature VWC Classification

Ensemble learning approaches are known for effectively extracting complementary features, when the base learners are chosen wisely [32–35]. In this study, an ensemble learning framework based on stacked generalization was developed to improve the robustness and generalization performance of spectroscopic classification. The proposed approach (Fig. 8) integrates multiple heterogeneous base learners; each trained on the proposed spectral index and complementary spectral features derived from selected wavelength regions. Combining heterogeneous classifiers allows the model to capture complementary spectral patterns that may not be fully represented by a single learning algorithm.

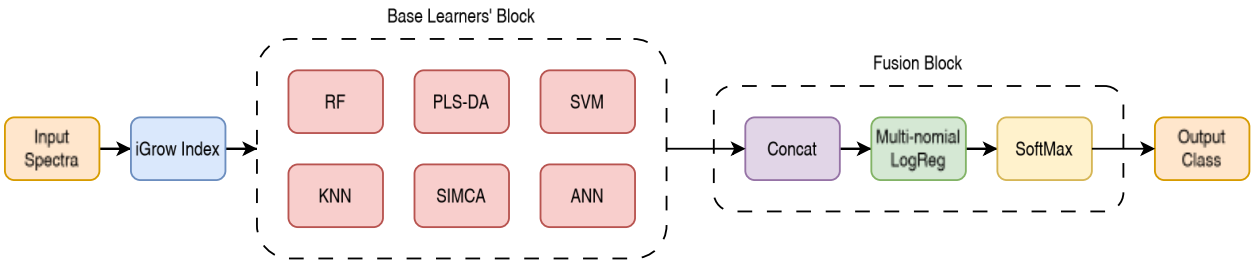


Fig. 8 – Architecture of the proposed MLSD model for VWC classification. The input reflectance spectrum is used to calculate RWI index which is utilized to train base learners; a fusion block is then trained on the out of fold results for decision making.

ALGORITHM 1: OPTIMAL WAVELENGTH TRIPLET FOR MULTIBAND DROUGHT INDEX

Inputs:

A set of reflectance measurements R *with wavelength column* W *and sample columns* S.
Global wavelength bounds $[W_{min}, W_{max}]$ *and step size* δW.
Wavelength search ranges $[A_{min}, A_{max}]$, $[B_{min}, B_{max}]$, $[C_{min}, C_{max}]$.
Classifier model $\mathbb{C}$ *and number of cross-validation folds* K

Outputs:

Optimal wavelength triplets $(\lambda_a\ \lambda_b\ \lambda_c)$
Ranked list of candidate triplets with cross validation accuracy mean and STD.

Load Data ← *Read spectral library file (e.g. CSV file)*

Initialize

Assign empty set of labeled samples $D \leftarrow \emptyset$.
Set wavelength column W *as spectral axis.*
Extract all sample columns $S = \{s_1, \dots, s_N\}$.
Assign zero to best score $S^* \leftarrow 0$.
Assign zero to best triplet $(\lambda_a^*\ \lambda_b^*\ \lambda_c^*) \leftarrow 0$.

Extract Labels – *For each sample column name s*:

Parse the θ *class label* y *from the column name.*
Add each sample to the set as a pair $D \leftarrow (\mathbf{R_s}, y_s)$, *where* **R**_*s is the reflectance spectrum*

Construct Candidate Wavelength Sets

Create a discrete wavelength grid $W = \{W_{min}, W_{min} + \delta W, \dots, W_{max}\}$
Create candidate set $A \leftarrow \{\forall\ w_i \in W \mid w_i \subseteq [A_{min}, A_{max}]\}$
Create candidate set B $\leftarrow \{\forall\ w_i \in W \mid w_i \subseteq [B_{min}, B_{max}]\}$
Create candidate set C $\leftarrow \{\forall\ w_i \in W \mid w_i \subseteq [C_{min}, C_{max}]\}$

Define Custom Drought Index

For any triplet $(\lambda_a\ \lambda_b\ \lambda_c)$ *compute* I_s $(\lambda_a\ \lambda_b\ \lambda_c)$ *for each sample* s *from Eq. (4)*

Search Triplets with Cross Validation – *For each triplet* $(\lambda_a\ \lambda_b\ \lambda_c) \in A \times B \times C$:

Compute the scalar feature vector $\mathbf{x} = [I_1, \dots, I_{|D|}]^T$.
Split data into train and test sets using input K.
Train classifier $\mathbb{C}$ *using stratified* K*-fold cross-validation.*
Compute the mean accuracy μ *and standard deviation* σ *across folds.*
Store the result $\{(\lambda_a\ \lambda_b\ \lambda_c), \mu, \sigma\}$.
If $\mu > S^*$ *update* $S^{\wedge} *\leftarrow \mu$ *and* $(\lambda_a^*\ \lambda_b^*\ \lambda_c^*) \leftarrow (\lambda_a\ \lambda_b\ \lambda_c)$.

Rank and Report

Sort all evaluated triplets in descending order of mean CV accuracy (μ).
Report the optimal triplet $(\lambda_a^*\ \lambda_b^*\ \lambda_c^*)$.

2.4.1 Partial Least Square Discriminant Analysis (PLS-DA)

PLS-DA is a supervised chemometric classification method derived from Partial Least Squares (PLS) regression and adapted for categorical response variables [36]. In PLS-DA, class membership is encoded as a binary response matrix, and PLS regression projects the predictor matrix (e.g., spectral data) onto a low-dimensional latent space that maximizes the covariance between predictors and class labels. Given a predictor matrix $\mathbf{X} \in \mathbb{R}^{n \times p}$ and a binary-coded response matrix $\mathbf{Y} \in \mathbb{R}^{n \times c}$, PLS-DA decomposes them as

$$\mathbf{X} = \mathbf{T}\mathbf{P}^T + \mathbf{E} \quad (6)$$

$$\mathbf{Y} = \mathbf{U}\mathbf{Q}^T + \mathbf{F} \quad (7)$$

where **T** and **U** are the score matrices, **P** and **Q** are loading matrices, and **E**, **F** represent the residual matrices. The latent variables in **T**are obtained by maximizing the covariance between **T**and **U**. Classification is then performed either by assigning samples to the class with the highest predicted response value or by applying a secondary classifier to the PLS score vectors.

2.4.2 Soft Independent Modeling of Class Analogy (SIMCA)

SIMCA is a class-modeling approach widely used in chemometrics [37–39], in which each class is modeled independently rather than directly discriminated against other classes. In practice, SIMCA is typically implemented using Principal Component Analysis (PCA) to describe the intrinsic variance structure of each class, followed by a

decision rule that assigns samples to classes based on their similarity to the corresponding PCA models. Given a predictor matrix $\mathbf{X} \in \mathbb{R}^{n \times p}$, PCA decomposes the data as

$$\mathbf{X} = \mathbf{T}\mathbf{P}^{\top} + \mathbf{E} \quad (8)$$

where **T** is the score matrix, **P** is the loading matrix, and **E** contains the residuals. A reduced number of principal components is retained to capture the dominant variance while reducing noise and collinearity. These PCA scores are then used as input to linear discriminant analysis (LDA), which seeks a linear transformation that maximizes the ratio of between-class scatter to within-class scatter. The LDA projection matrix **W** is obtained by solving

$$\mathbf{W} = \arg\max_{\mathbf{W}} \frac{\mathbf{W}^{\top}\mathbf{S}_B\mathbf{W}}{\mathbf{W}^{\top}\mathbf{S}_W\mathbf{W}} \quad (9)$$

where $\mathbf{S}_B$ and $\mathbf{S}_W$ denote the between-class and within-class scatter matrices, respectively. Classification is performed by assigning samples to the class with the highest posterior probability under the LDA model.

2.4.3 Support Vector Machines (SVM)

SVMs are supervised learning models widely used in spectral analysis for both classification and regression tasks, particularly well-suited for high-dimensional and collinear spectral datasets [40–42]. The core idea of SVM is to determine an optimal decision boundary that maximizes the margin between classes, thereby improving model generalization. Given a training set $\{(\mathrm{x}_i, y_i)\}_{i=1}^{n}$ with input features $\mathrm{x}_i \in \mathbb{R}^p$ and class labels $y_i \in \{-1, +1\}$, SVM solves the following optimization problem:

$$\min_{\mathrm{w},b,\xi} \ \frac{1}{2} \| \mathrm{w} \|^2 + C \sum_{i=1}^{n} \xi_i \quad (10)$$

subject to

$$y_i(\mathrm{w}^{\top}\phi(\mathrm{x}_i) + b) \geq 1 - \xi_i \ , \ \xi_i \geq 0 \quad (11)$$

where $\phi(\cdot)$ is a nonlinear mapping induced by a kernel function, ξ are slack variables allowing misclassification, and C is a regularization parameter controlling the trade-off between margin maximization and classification error. In this study, the radial basis function (RBF) kernel was used.

2.4.4 Random Forest Algorithm

Random forest (RF) is an ensemble learning method that constructs multiple decision trees during training and outputs the vote of the majority of the trees for classification tasks [43]. Additionally, RF provides an estimate of feature importance based on impurity reduction. This makes it particularly useful for dimensionality reduction in spectral data, as the most informative wavelengths can be identified. The importance of feature j is defined by Eq.(12)

$$Importance(j) = \frac{1}{T} \sum_{t=1}^{T} \sum_{s \in S_{j,t}} \frac{N_s}{N} \Delta i(s) \quad (12)$$

where T is the total number of trees in the forest, $S_(j,t)$ is the set of all splits in tree t using feature j, N is the total number of samples, N_s is the number of samples at node s, and $\Delta i(s)$ is the impurity reduction at split s given by Eq.(13):

$$\Delta i(s) = i_{parent} - \left(\frac{n_L}{n} i_L + \frac{n_R}{n} i_R\right) \quad (13)$$

Eq.(13) describes the impurity reduction when a node with impurity i_{parent} is split into two child nodes (left and right), where n, n_L, n_R represent number of samples in the parent, left, and right nodes, respectively, and i_L, i_R denote the impurity of the left and right child nodes, respectively. In this study, the Gini impurity metric was used to evaluate node impurity, defined by Eq. (14)

$$G = 1 - \sum_{i=1}^{C} p_i^2 \quad (14)$$

where C is the total number of classes and p_i is the probability of class i at the node.

2.4.5 Multi-Learner Spectral Drought Model

To integrate the predictions of multiple base classifiers, a stacked generalization ensemble learning strategy was employed. Ensemble learning can improve spectroscopic classification by combining models that capture complementary spectral patterns and decision boundaries. The base classifiers including PLS-DA, SIMCA, SVM, KNN, ANN, and RF were trained on the input features, and their predictions were subsequently used as inputs to a higher-level meta-model, referred to as the Multi-learner Spectral Drought (MLSD) model. To prevent information leakage, the MLSD meta-model was trained exclusively using predictions obtained from cross-validated base learners. Furthermore, an ablation study was conducted to identify the most influential base learners and optimize the MLSD architecture.

A multinomial logistic regression model was selected as the meta-classifier due to its effectiveness in learning linear combinations of probabilistic outputs from heterogenous classifiers. Each base classifier M produced class probability estimates $P_m(y = k \mid \mathbf{x})$ for class k, where $m = 1, \dots, M$. These probabilities were concatenated to form a meta-feature vector defined by Eq. (15)

$$\mathbf{z}(\mathbf{x}) = [P_1(y = 1 \mid \mathbf{x}), \dots, P_1(y = K \mid \mathbf{x}), \dots, P_M(y = 1 \mid \mathbf{x}), \dots, P_M(y = K \mid \mathbf{x})] \quad (15)$$

The MLSD then estimated the final class probabilities using a SoftMax model,

$$P(y = k \mid \mathbf{z}) = \frac{\exp(\boldsymbol{\beta}_k^\top \mathbf{z})}{\sum_{j=1}^{K} \exp(\boldsymbol{\beta}_j^\top \mathbf{z})} \quad (16)$$

where $\boldsymbol{\beta}_k$ denotes the parameter vector associated with class k. The predicted class label is determined by selecting the class with the highest posterior probability. By leveraging complementary decision patterns across base learners, the stacking approach provided a data-driven mechanism for improving classification accuracy in spectroscopic analysis.

Lastly, A systematic ablation study was conducted to analyse the contribution and interaction of individual base learners within the proposed stacking ensemble that can be found in the Appendix I. Two complementary ablation strategies were applied. First, a leave-one-learner-out ablation was performed, in which each base model was removed from the ensemble, one at a time, while all other learners were retained. This experiment quantified the marginal contribution of each learner to the overall model performance. Second, an add-one-learner ablation was conducted, where base learners were incrementally added to the ensemble starting from a single model. This procedure allowed the evaluation of performance growth and the identification of synergistic effects among complementary learners. Together, these ablation experiments provide insight into a) the importance of each learner within the ensemble and b) the cumulative benefit of ensemble diversity.

2.5 Robotic LiDAR-Based Moisture Sensing

To investigate the possibility of using a compact off-the-shelf sensor for estimating VWC in horticultural rockwool, a LiDAR camera was mounted on a robotic manipulator. The system enabled controlled, repeatable, non-contact measurements of full-size rockwool cubes under varying moisture conditions. A multi-modal approach was used by combining RGB, active infrared, and depth for moisture estimation and calibration under various conditions. The following subsections describe the robotic setup, experimental design, data acquisition, and feature extraction pipeline used for VWC classification.

2.5.1 *Robotic Platform and Sensor Configuration*

An Intel RealSense L515 LiDAR camera was mounted on the end effector of a modified Robotis Open ManipulatorX arm installed on a Robotis WaffleBot to enable non-contact sensing of horticultural rockwool cubes (Fig. 9). For this setup, the standard Open ManipulatorX was modified by a) replacing the original links with 3D printed links (increasing the length from 8 to 42 cm) and b) replacing the end-effector gripper with a 3D printed mount for LiDAR camera and spectroradiometer sensor. The L515 provided spatially aligned RGB images, active near-infrared intensity, and depth data, the sensor was positioned facing the exposed surface of each cube. The embedded laser had a wavelength range of $844 - 875\,nm$, depending on the operating temperature $(0 - 50℃)$, and the depth was calculated internally based on time-of-flight (ToF). Apogee MS-100 handheld spectroradiometer was mounted with the sensor facing the direction same direction as LiDAR camera and the provided the environment illumination (lux) measurement. Mobile base position and arm pose were controller by tele-operation using ROS2 and RVIS environment running on a Jetson Orin Nano connected to OpenCR control board. The robot remained stationary during each acquisition to minimize motion-induced errors.

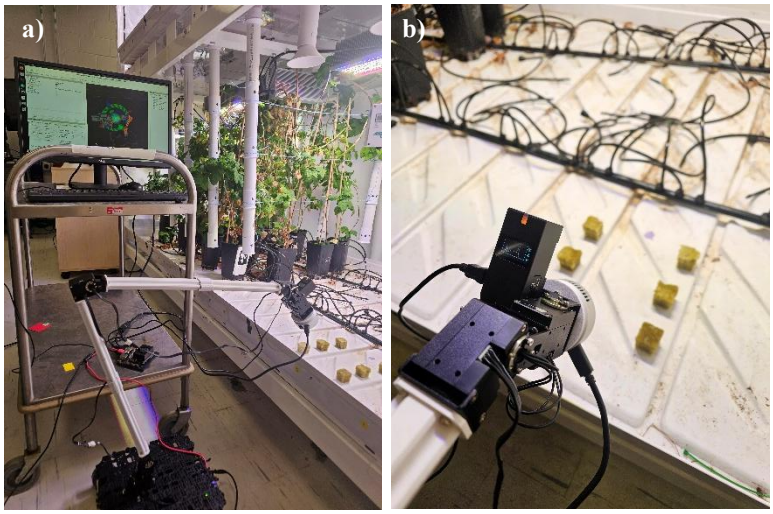


Fig. 9 – Mobile robot and sensor configuration setup: a) mobile base and modified arm during an inference session b) Spectroradiometer and LiDAR installed at the end-effector of the arm.

2.5.2 *Rockwool Cubes Preparation*

A total of 100 full-size horticultural rockwool cubes with approximate dimensions of $2.5 \times 2.5 \times 2.5\ cm^3$ were used. The cubes had an initial dry mass of $5.17\ \pm 0.58$ and a saturated wet mass of 64.31 ± 7.42 grams. Each cube was weighed before sensing to establish its reference moisture content through Eq.(2). Three VWC levels, namely $\{0, 23.9 \pm 3.5\%, 50.4 \pm 3.1\%\}$, were used for data collection and calibration. The cubes were independently prepared and identified to support cube-level separation during model validation.

2.5.3 *Experimental Conditions and Data Acquisition*

Measurements were collected under controlled variations in VWC, sensor distance, and ambient illumination. Measurements were made at sensor-to-target distances of $\{0.5, 0.6, 0.7\}$ meters, and illumination levels of $\{50, 150, 250\}$ lux, approximately. For each combination of conditions, the robot positioned the L515 at the predefined measurement pose and acquired 120 frames after a stabilization period of 3 seconds. A total of 2700 observations were obtained across 3 acquisition sessions.

2.5.4 *Data Preprocessing*

The rockwool surface was isolated in each RGB image using a colour-based segmentation method. The resulting mask was transferred to the spatially aligned infrared, and depth images to define a common region of interest (ROI).

Background pixels, invalid depth measurements, and pixels with confidence values below 90% were excluded. To reduce boundary effects from entering the analysis, the extracted ROI was reduced inward by 5% from each boundary. The same ROI was used across all modalities for each observation.

RGB values of each pixel within the valid ROI were extracted and averaged over the 120 frames, from which the mean, standard deviation of each channel were calculated. Although they were not treated as direct narrowband measurements of the 570 nm wavelength identified through spectroscopy, these features represented changes in the visible appearance of rockwool. Similarly, near-infrared channel within the ROI was averaged over the frames and was utilized as a more water sensitive sensing modality. Sensor distance, and ambient illumination were retained as acquisition-condition variables. All features were standardized using parameters calculated exclusively from the training data.

2.5.5 Multimodal VWC Classification

An RBF-SVM classifier was developed to estimate the VWC class from the combined RGB, active-infrared, depth, and ambient illumination features. Model hyperparameters were optimized using Bayesian hyperparameter optimization within the training data. To prevent information leakage, grouped stratified cross-validation based on cube ID was utilized, followed by an independent test set.

Feature-ablation experiments were performed starting with RGB and by adding NIR, depth, and illumination sequentially. This analysis was used to determine the contribution of each sensing modality and establish whether classification performance resulted primarily from moisture-sensitive measurements rather than experimental conditions. Model performance was evaluated using precision, recall, F1-score.

2.6 Evaluation Metrics

To establish a baseline for evaluating the proposed 1D-CNN network and MLSD models, several widely used machine learning models in chemometric analysis were trained using the classical NMDI and the tailored RWI spectral index for VWC classification. The 1D-CNN was trained on the full spectra, leaving the feature selection to the network, whereas ML models were trained on the engineered indices. To prevent information leakage between training and testing stages, the MLSD model was trained using cross-validated predictions from the base classifiers.

Spectral data within each class were randomly split into training (80%) and testing (20%) subsets and were labeled based on VWC level and sample identifier, ensuring that spectra originating from the same sample were not included in both training and testing sets. The experiments were repeated using a 5-fold cross-validation procedure, and the mean and standard deviation of the performance metrics were reported. To quantify model performance, Precision (P), Recall (R), and F1-Score (F1) were used as evaluation metrics.

$$\mathrm{P} = \frac{\mathrm{TP}}{\mathrm{TP} + \mathrm{FP}} \tag{17}$$

$$\mathrm{R} = \frac{\mathrm{TP}}{\mathrm{TP} + \mathrm{FN}} \tag{18}$$

$$\mathrm{F}_1 = 2 \times \frac{\mathrm{P} \times \mathrm{R}}{\mathrm{P} + \mathrm{R}} \tag{19}$$

Precision (Eq. 17) is defined as the ratio of true positives (TP) to the sum of true positives and false positives (FP). Recall (Eq. 18) represents the proportion of actual positive instances correctly identified by the model and is calculated as the ratio of true positives to the sum of true positives and false negatives (FN). The F1-Score (Eq. 19) is the harmonic mean of precision and recall, providing a single performance measure that balances false positives and false negatives.

3 Results and Discussion

3.1 Spectral Library

To construct a spectral library of rockwool reflectance, reflectance measurements were collected at approximately 5% increments of VWC levels for 100 samples. To illustrate the spectral characteristics of rockwool, the average reflectance spectrum was calculated for each VWC level and plotted across the wavelength range (Fig. 9).

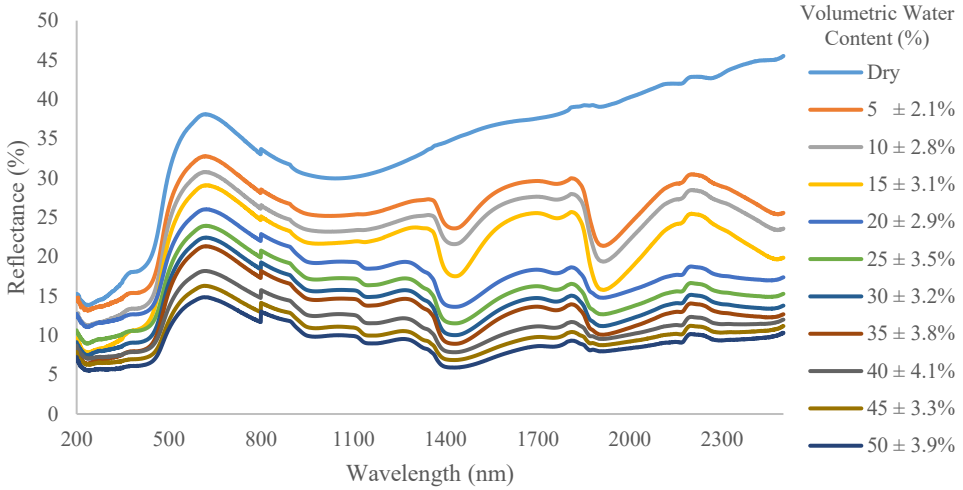


Fig. 10 – Averaged reflectance spectra of rockwool cubes from 200-2500 nm at different volumetric water content levels.

Fig. 9 shows that reflectance values decrease with increasing water content, with the near-infrared bands and shortwave infrared regions showing greater sensitivity than the visible and ultraviolet regions. The largest reflectance differences between moisture levels were observed in the NIR–SWIR wavelength range. At low VWC levels, reflectance decreases sharply, while the rate of change becomes smaller at higher VWC levels. Similar moisture-dependent reflectance behavior has been reported previously for soil substrates [18].

3.2 Rockwool Water Index (RWI)

To enable low-dimensional yet discriminative characterization of VWC in rockwool substrates, a wavelength selection strategy was employed to derive a compact spectral index. Algorithm 1 was used to systematically evaluate all possible three-band wavelength combinations. The triplet that maximized multi-class VWC classification accuracy was identified as (570 nm, 1560 nm, 1940 nm). The resulting normalized multiband spectral index, termed RWI, is defined as:

$$\mathrm{RWI} = \frac{\mathrm{R}_{570} - (\mathrm{R}_{1560} - \mathrm{R}_{1940})}{\mathrm{R}_{570} + (\mathrm{R}_{1560} - \mathrm{R}_{1940})} \quad (21)$$

The selected wavelengths correspond to spectral regions with distinct physical relevance. Reflectance at 570 nm lies in the visible range and primarily reflects substrate scattering and structural properties, which are relatively insensitive to water content. In contrast, 1560 nm and 1940 nm are located in the shortwave infrared region associated, which contain strong and moderate water absorption features, respectively. The difference term $(R_{1560} - R_{1940})$ therefore enhances sensitivity to moisture-dependent absorption changes, while normalization by the sum reduces sensitivity to illumination variability and overall reflectance magnitude.

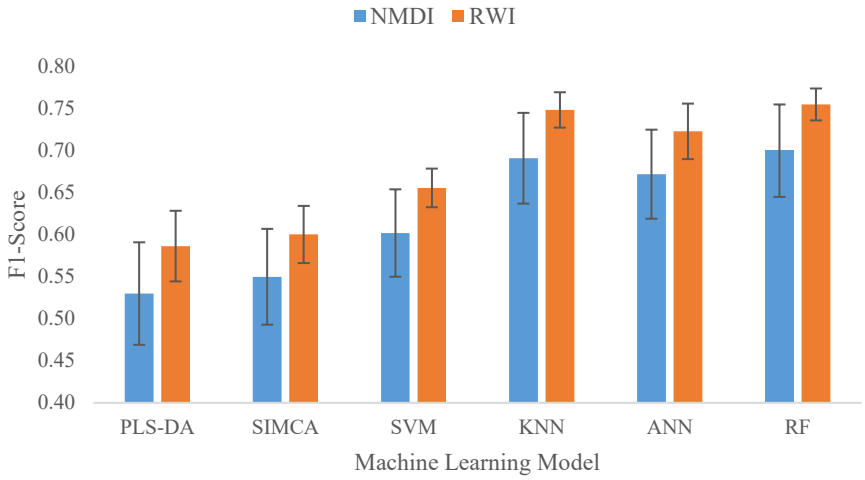


Fig. 11 – Performance comparison of machine learning models for VWC classification in rockwool using NMDI versus RWI as input features. Results correspond to the mean F1-score across all classes obtained from 5-fold cross-validation.

To analyze the effectiveness of the proposed index (RWI), PLS-DA, SIMCA, SVM, KNN, ANN, and RF classifiers were first trained using NMDI to establish a baseline and subsequently trained using RWI. As illustrated in Fig. 10, models trained using RWI achieved higher mean F1-scores and lower standard deviations compared with the same models trained using NMDI. Among the tested models, PLS-DA achieved the lowest performance, with F1-scores of approximately 53% using NMDI and 59% using RWI. KNN and RF achieved the highest classification performance, improving by 5-6% when trained with RWI. Specifically, KNN increased from an F1≅69% to 75%, while RF improved from F1≅71% to 76%. These results indicate that the proposed RWI index provides a compact and discriminative spectral representation for rockwool VWC classification. Because the index relies on only three wavelengths, it may be implemented using low-cost multispectral or narrowband sensing systems, which supports potential deployment for real-time irrigation monitoring in controlled-environment agriculture.

3.3 Spectral-based VWC Classification

To provide a comprehensive comparison between models, precision, recall, and F1-score were first macro-averaged across all VWC classes, further, a 5-fold cross-validation was performed and the mean and standard deviation were reported. Fig. 11 summarizes the performance of all evaluated models, whereas Table 2 reports the corresponding numerical results.

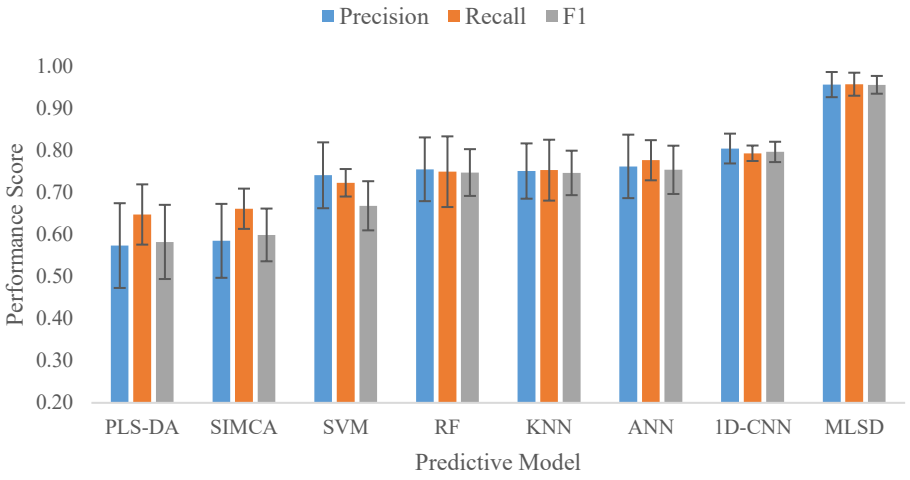


Fig. 12 – Performance comparison of baseline classifiers and the proposed 1D-CNN and MLSD models for VWC classification in rockwool substrate. Metrics represent average values across all classes obtained from 5-fold cross-validation.

Among the classical machine learning models trained on the RWI index, tree-based and instance-based algorithms achieved higher performance than linear or projection-based approaches. Specifically, RF, KNN and ANN achieved mean F1-scores of 74.8%, 74.71%, and 75.45%, respectively, whereas SVM, SIMCA, and PLS-DA achieved 66.89%, 59.95% and 58.29%. This result suggests that nonlinear decision boundaries and local neighborhood relationships provide advantages when using the RWI index representation. In contrast, PLS-DA and SIMCA, which rely primarily on linear projections and variance-based modeling, showed lower classification performance. This likely reflects overlapping class distributions and nonlinear transitions between VWC levels within the spectral data.

Table 2 – Performance of the proposed models and baseline machine learning classifiers averaged across all VWC classes.

Model	Precision			Recall			F1		
PLS-DA	0.5742	±	0.1008	0.6482	±	0.0717	0.5829	±	0.0883
SIMCA	0.5855	±	0.0880	0.6618	±	0.0479	0.5995	±	0.0627
SVM	0.7415	±	0.0784	0.7236	±	0.0327	0.6689	±	0.0585
RF	0.7557	±	0.0758	0.7500	±	0.0841	0.7480	±	0.0556
KNN	0.7515	±	0.0658	0.7536	±	0.0725	0.7471	±	0.0529
ANN	0.7626	±	0.0755	0.7773	±	0.0477	0.7545	±	0.0575
1D-CNN (Proposed)	0.8051	±	0.0355	0.7939	±	0.0184	0.7971	±	0.0242
MLSD (Proposed)	**0.9573**	**±**	**0.0299**	**0.9582**	**±**	**0.0274**	**0.9567**	**±**	**0.0212**

The proposed 1D-CNN and MLSD models achieved mean F1-scores of 79.71% and 95.67%, respectively. Relative to the best-performing baseline models (RF and ANN), the 1D-CNN improved the F1-score by 4.3%, whereas the MLSD model improved performance by 15.9%. The primary difference between the proposed models lies in input representation and feature extraction strategy. The 1D-CNN processes the full spectrum signature and performs feature extraction internally through convolutional operations whereas MLSD and the classical machine learning models use the RWI index together with a narrow spectral window (±5 nm around the selected wavelengths) as input features. The 1D-CNN achieved higher F1-scores than RF and ANN, indicating that the convolutional structures are effective for extracting informative patterns from hyperspectral data. However, the improvement over the best baseline models is modest. This is likely due to the limited dataset size, as deep learning models typically require larger datasets to fully exploit their representational capacity. The class-level performance of the MLSD model in detecting each VWC class is illustrated in Fig. 12, and the corresponding row-normalized confusion matrix is presented in Fig. 13. The

confusion matrix indicates that the model correctly classifies most VWC levels with high accuracy ($P > 0.9$), particularly at lower and higher moisture levels. Misclassification is primarily observed between the 35% and 40% VWC classes, where the spectral signatures are more similar and the class boundaries overlap.

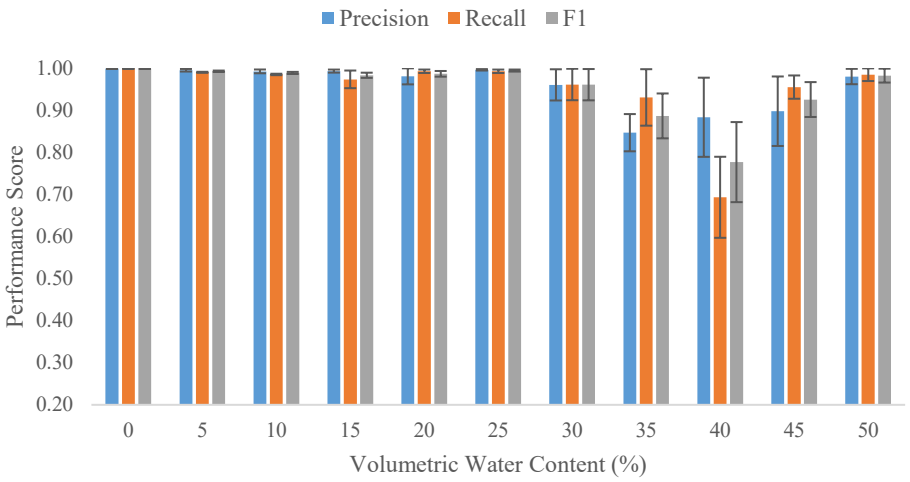


Fig. 13 – Classification performance of the MLSD model across VWC levels obtained from 5-fold cross-validation

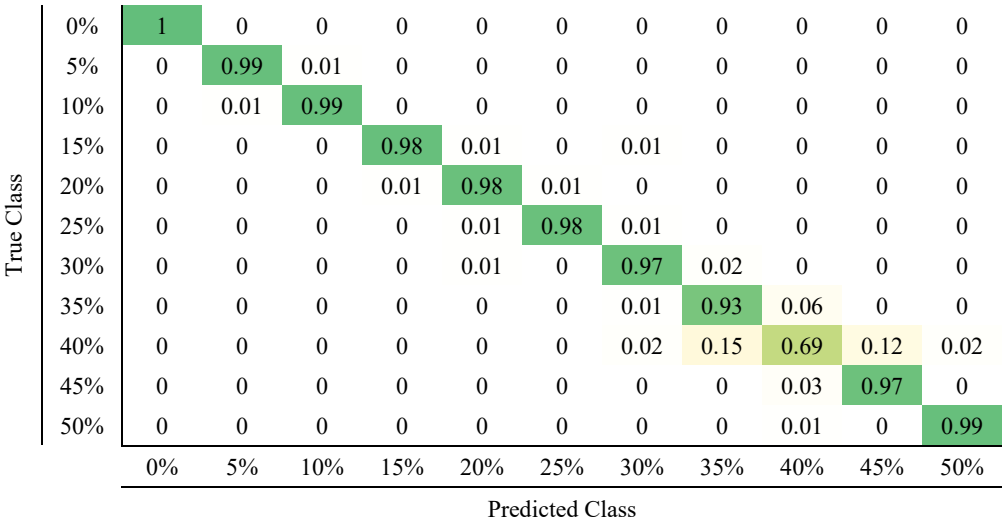


Fig. 14 – Row-normalized confusion matrix of the MLSD, averaged across 5-fold cross-validation results.

3.4 LiDAR-based VWC Classification

Table 3 presents the classification performance obtained using different combinations of sensing modalities. The RGB-only model produced the lowest performance, as expected, with $F_1 \approx 59\%$. This indicates that visible appearance alone provided some moisture-related information but was insufficient for reliable separation of the VWC classes. Adding active NIR information substantially improved the F1-score to 77.12%, demonstrating that the infrared return captured complementary moisture-dependent variations that were not fully represented by RGB data. The inclusion of depth further increased precision and recall to 91.32% and 86.25%, respectively. This improvement suggests that sensor o target distance influences sensor readings significantly. The complete feature set, incorporating RGB, NIR, depth, and illumination, achieved the best overall performance, with a precision of 92.89%. It also produced lower variability than the other configurations, indicating more consistent classification across validation folds. Illumination provided only a modest improvement over the RGB–NIR–depth configuration, which confirms the independence of NIR from the illumination.

Table 3 – Classification performance obtained using different sensing modalities of L515 LiDAR, averaged over all classes and folds.

Feature	Precision			Recall			F1		
RGB	0.6341	±	0.0583	0.5514	±	0.0647	0.5899	±	0.0563
RGB+NIR	0.7916	±	0.0436	0.7518	±	0.0468	0.7712	±	0.0483
RGB+NIR+Depth	0.9132	±	0.0226	0.8625	±	0.0354	0.8871	±	0.0362
RGB+NIR+Depth+Illumination	0.9289	±	0.0221	0.8911	±	0.0316	0.9096	±	0.0311

The confusion matrix from the RBF-SVM classifier is provided in Fig. 14. The two experimental stages demonstrate a progression from controlled spectral characterization to practical robotic sensing. Laboratory spectroscopy identified moisture-dependent reflectance patterns across the UV–Vis–NIR range and enabled the selection of a compact wavelength combination for rockwool VWC classification. However, the L515 does not directly measure the optimized 570, 1560, and 1940 nm wavelengths. Therefore, the robotic experiment should not be interpreted as a direct implementation of the proposed RWI. Instead, it evaluates whether moisture-related optical changes remain detectable using the lower-dimensional sensing modalities available in a commercially deployable system.

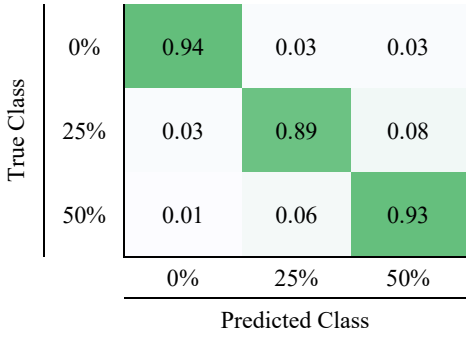


Fig. 15 – Confusion matrix obtained from the LiDAR-based VWC classification, averaged over 5-fold cross validation

4 Conclusion

This study presented a laboratory-to-robotic-deployment framework for non-invasive classification of volumetric water content (VWC) in horticultural rockwool. High-resolution UV–Vis–NIR spectroscopy was first combined with wavelength optimization, machine learning, and deep learning to characterize moisture-dependent spectral variations. A material-specific rockwool water index (RWI) outperformed the conventional NMDI, demonstrating the advantage of developing indices tailored to the optical properties of the target substrate.

The full-spectrum 1D-CNN improved the mean F1-score by 4.3% relative to the strongest baseline classifier. The proposed MLSD ensemble, comprising RF, PLS-DA, and SIMCA base learners with a multinomial logistic regression meta-classifier, achieved a mean F1-score of 95.8%, representing a 15.9% improvement over the baseline. Despite using only approximately 1.3% of the available spectral bands, MLSD outperformed the full-spectrum 1D-CNN, demonstrating the effectiveness of optimized wavelength selection and heterogeneous ensemble learning.

The laboratory findings were subsequently extended to robot-mounted LiDAR sensing of full-size rockwool cubes. The multi-modal model using RGB, NIR, depth, and illumination features achieved averaged precision of 92.89%. The confusion matrix confirms the ability to use a compact sensor for VWC classification, although it is limited to only three classes in comparison to the use of an advanced sensor that granted high-precision 11-class classification. Progressive improvements from RGB-only to the complete feature set demonstrated that visible, active-infrared, geometric, and environmental information contributed complementary information to moisture classification.

Overall, the results establish a practical progression from detailed spectral characterization to compact multimodal robotic sensing. Although the LiDAR does not directly measure the wavelengths used in RWI, it demonstrates that

moisture-related information can be recovered using a commercially available standoff sensor. Future work should evaluate additional VWC levels, substrates, cultivation conditions, and unseen samples and integrate the framework with closed-loop robotic irrigation.

Statements and Declarations

Competing interests

The authors declare that they have no known competing interests.

Funding

This work was supported by Weston Family Foundation via Homegrown Innovation Challenge [grant number: SA-10691 to LGC and HB], and NSERC Grants [RGPIN-2019-05780 to LGC; RGPIN-2019-05615 to HB, RGPIN-2019-05562 to KZ]

Authorship contributions

Parham Jafary: Conceptualization, Data curation, Formal analysis, Investigation, Methodology, Software, Validation, Visualization, Writing – original draft, Writing – review & editing.

Kourosh Zareinia: Conceptualization, Supervision, Funding acquisition, Resources, Writing – review & editing**.**

Lesley G. Campbell: Conceptualization, Formal analysis, Funding acquisition, Methodology, Project administration, Resources, Supervision, Writing – review & editing.

Habiba Bougherara: Conceptualization, Funding acquisition, Resources, Supervision, Writing – review & editing.

Data availability

Data will be made available upon request.

Acknowledgements

The authors gratefully acknowledge Teymour Amirov for designing and fabricating the custom 3D-printed slicing tool, as well as for his support in the preparation of rockwool samples used in this study. The authors also would like to thank Michelle Pham and Anna Bazangeya for their assistance with preliminary rockwool spectroscopy experiments, which helped inform and refine the subsequent experimental design.

Appendix I: Ablation Study of MLSD

Ablation study results are summarized in Table 4. The results of the leave-one-learner-out ablation suggested that several base learners may introduce partial redundancy, as removing most individual learners resulted in only minor changes in overall performance. The primary exception was SIMCA, which, despite achieving relatively low standalone performance (F1≈60%), produced the largest reduction in ensemble performance when removed (ΔF1≈ −1.7%). This observation indicates that SIMCA contributes complementary discriminative information rather than raw predictive accuracy, highlighting the importance of model diversity in stacking ensembles. The add-one-learner ablation was then used to further investigate potential redundancy among base learners. The variants began with RF, which achieved an F1-score of 87.85% within the MLSD architecture. This result highlights the impact of the stacking fusion stage, as the RF-based variant performed approximately 13% higher than the standalone RF classifier (F1≈75%). When the strongest individual classifiers (KNN, ANN, and SVM) were added to the ensemble, the improvement in performance was relatively small. In contrast, adding PLS-DA and SIMCA increased classification accuracy by 3.1% and 4.1%, respectively, demonstrating that these learners contribute complementary information to the ensemble. Subsequent variants that incorporated SVM, KNN, and ANN did not produce meaningful improvements in the overall

accuracy, F1 score, or standard deviation, suggesting that these learners do not significantly enhance either predictive performance or robustness of the final model. Based on these results, the combination of RF, PLS-DA, and SIMCA, together with the multivariate logistic regression meta-classifier, was selected as the optimal configuration of the MLSD model. These results indicate that ensemble diversity, rather than the inclusion of the individually strongest learners, plays a key role in maximizing classification performance for spectral moisture analysis.

Table 4 – Ablation study for base learner choices.

Ablation	Base Learner Variant	Accuracy			F1		
Leave One Learner Out	Full	0.9527	±	0.0052	0.9507	±	0.0056
	- SIMCA	0.9364	±	0.0116	0.9340	±	0.0118
	- PLSDA	0.9501	±	0.0056	0.9478	±	0.0061
	- RF	0.9564	±	0.0100	0.9545	±	0.0110
	- KNN	0.9518	±	0.0076	0.9499	±	0.0083
	- ANN	0.9536	±	0.0081	0.9511	±	0.0087
	- SVM	0.9518	±	0.0052	0.9496	±	0.0058
Add One Learner	RF	0.8803	±	0.0104	0.8785	±	0.0103
	RF+KNN	0.9106	±	0.0162	0.9085	±	0.0172
	RF+KNN+ANN	0.9282	±	0.0111	0.9261	±	0.0117
	RF+KNN+ANN+SVM	0.9318	±	0.0125	0.9291	±	0.0134
	RF+PLSDA	0.9118	±	0.0133	0.9097	±	0.0131
	RF+PLSDA+SIMCA	**0.9527**	**±**	**0.0052**	**0.9567**	**±**	**0.0054**
	RF+PLSDA+SIMCA+SVM	0.9555	±	0.0067	0.9536	±	0.0071
	RF+PLSDA+SIMCA+SVM+KNN	0.9536	±	0.0081	0.9511	±	0.0087
	RF+PLSDA+SIMCA+SVM+KNN+ANN	0.9527	±	0.0052	0.9507	±	0.0056

References

1. Khan AA, Wang Y-F, Akbar R, Alhoqail WA (2025) Mechanistic insights and future perspectives of drought stress management in staple crops. Front Plant Sci 16:1547452
2. Venkatasaichandrakanth P, Iyapparaja M (2024) A survey on pest detection and classification in field crops using artificial intelligence techniques. Int J Intell Robot Appl 8:709–734. https://doi.org/10.1007/s41315-024-00347-w
3. Jafary P, Campbell LG, Bazangeya A, et al (2026) Phenology-based learning framework for yield estimation and harvest forecasting of raspberry fruits. Int J Intell Robot Appl. https://doi.org/10.1007/s41315-026-00564-5
4. Tobias J, Lim SH, Duke M, et al (2025) Implementation of an autonomous mobile platform for agricultural tasks in corridor-like environments. Int J Intell Robot Appl 9:389–409. https://doi.org/10.1007/s41315-024-00386-3
5. Ansari S, Gohil MK, Maeda Y, Bhattacharya B (2026) Design and development of a new hybrid auxetic gripper system for adaptive precision tomato harvesting. Int J Intell Robot Appl 10:60–83. https://doi.org/10.1007/s41315-025-00488-6
6. Crow WT, Kustas WP, Prueger JH (2008) Monitoring root-zone soil moisture through the assimilation of a thermal remote sensing-based soil moisture proxy into a water balance model. Remote Sens Environ 112:1268–1281. https://doi.org/https://doi.org/10.1016/j.rse.2006.11.033
7. Li M, Sun H, Zhao R (2023) A Review of Root Zone Soil Moisture Estimation Methods Based on Remote Sensing. Remote Sens (Basel) 15:5361. https://doi.org/10.3390/rs15225361

8. Babaeian E, Paheding S, Siddique N, et al (2021) Estimation of root zone soil moisture from ground and remotely sensed soil information with multisensor data fusion and automated machine learning. Remote Sens Environ 260:112434. https://doi.org/https://doi.org/10.1016/j.rse.2021.112434
9. Blok C (1999) AIR/WATER MANAGEMENT IN ROCKWOOL SLABS. Acta Hortic 79–88. https://doi.org/10.17660/ActaHortic.1999.481.5
10. Wakoh H, Haggett BGD (1996) Automated Measurement of Water Content and Nutrient Concentration in Rockwool Slabs. Journal of Agricultural Engineering Research 65:29–35. https://doi.org/10.1006/jaer.1996.0077
11. Thomas P, Knox OGG, Powell JR, et al (2023) The Hydroponic Rockwool Root Microbiome: Under Control or Underutilised? Microorganisms 11:835. https://doi.org/10.3390/MICROORGANISMS11040835
12. Goodchild MS, Jenkins MD, Whalley WR, Watts CW (2018) A novel dielectric tensiometer enabling precision PID-based irrigation control of polytunnel-grown strawberries in coir. Biosyst Eng 165:70–76. https://doi.org/10.1016/j.biosystemseng.2017.10.018
13. Kang S, van Iersel MW, Kim J (2019) Plant root growth affects FDR soil moisture sensor calibration. Sci Hortic 252:208–211. https://doi.org/10.1016/j.scienta.2019.03.050
14. Sarić R, Nguyen VD, Burge T, et al (2022) Applications of hyperspectral imaging in plant phenotyping. Trends Plant Sci 27:301–315. https://doi.org/10.1016/J.TPLANTS.2021.12.003
15. Burnett AC, Serbin SP, Davidson KJ, et al (2021) Detection of the metabolic response to drought stress using hyperspectral reflectance. J Exp Bot 72:6474–6489. https://doi.org/10.1093/jxb/erab255
16. El Azizi S, Amharref M, Bernoussi A (2024) Assessment of Water Content in Plant Leaves Using Hyperspectral Remote Sensing and Chemometrics, Application: Rosmarinus officinalis. Journal of Biosystems Engineering 49:337–345. https://doi.org/10.1007/s42853-024-00236-x
17. Cardoso Jesus JL, Bilhalva N dos S, Santana DC, et al (2026) Classification of the Physicochemical Quality of White, Parboiled, Black and Red Rice in Storage and Processing Units Integrating Near-infrared Spectroscopy, Hyperspectral Sensing, and Machine Learning Models. Journal of Biosystems Engineering 51:8. https://doi.org/10.1007/s42853-025-00290-z
18. Wang L, Qu JJ (2007) NMDI: A normalized multi-band drought index for monitoring soil and vegetation moisture with satellite remote sensing. Geophys Res Lett 34:. https://doi.org/10.1029/2007GL031021
19. Döpper V, Rocha AD, Berger K, et al (2022) Estimating soil moisture content under grassland with hyperspectral data using radiative transfer modelling and machine learning. International Journal of Applied Earth Observation and Geoinformation 110:102817. https://doi.org/10.1016/j.jag.2022.102817
20. Alipourvarmazabadi M, Ebner M (2026) Robot localization: a comprehensive survey from classical methods to intelligent autonomy. Int J Intell Robot Appl. https://doi.org/10.1007/s41315-026-00528-9
21. Liu X, Liu Z, Kong F, Zhang F (2023) Large-Scale LiDAR Consistent Mapping Using Hierarchical LiDAR Bundle Adjustment. IEEE Robot Autom Lett 8:1523–1530. https://doi.org/10.1109/LRA.2023.3238902
22. Saha A, Dhara BC (2024) 3D LiDAR-based obstacle detection and tracking for autonomous navigation in dynamic environments. Int J Intell Robot Appl 8:39–60. https://doi.org/10.1007/s41315-023-00302-1
23. Sasaki H, Komeno N, Hachimine T, et al (2026) Robotic system for chemical experiment automation with dual demonstration of end-effector and jig operations. Int J Intell Robot Appl 10:84–106. https://doi.org/10.1007/s41315-025-00492-w
24. Dorigoni D, Shamsfakhr F, Pincheira M, et al (2024) Fostering Precision Agriculture through Affordable 3D LiDAR Deskewing with EKF. In: 2024 IEEE Sensors Applications Symposium (SAS). pp 1–6
25. Zhang C, Chen M, Wang G, et al (2026) A fast and robust 3D LiDAR-based loop closure detection method using BEV images. Int J Intell Robot Appl 10:642–659. https://doi.org/10.1007/s41315-025-00516-5
26. Hossain S, Lin X (2025) Enhancing mapping precision in autonomous delivery robots through tightly-coupled fusion of uncertainty-aware GPS and LiDAR odometry. Int J Intell Robot Appl 9:439–453. https://doi.org/10.1007/s41315-024-00397-0
27. Tan K, Cheng X, Ding X, Zhang Q (2016) Intensity Data Correction for the Distance Effect in Terrestrial Laser Scanners. IEEE J Sel Top Appl Earth Obs Remote Sens 9:304–312. https://doi.org/10.1109/JSTARS.2015.2497310
28. Hofle B (2014) Radiometric Correction of Terrestrial LiDAR Point Cloud Data for Individual Maize Plant Detection. IEEE Geoscience and Remote Sensing Letters 11:94–98. https://doi.org/10.1109/LGRS.2013.2247022
29. Victor N, Maddikunta PKR, Mary DRK, et al (2024) Remote Sensing for Agriculture in the Era of Industry 5.0—A Survey. IEEE J Sel Top Appl Earth Obs Remote Sens 17:5920–5945. https://doi.org/10.1109/JSTARS.2024.3370508

30. Gao BC (1996) NDWI—A normalized difference water index for remote sensing of vegetation liquid water from space. Remote Sens Environ 58:257–266. https://doi.org/10.1016/S0034-4257(96)00067-3
31. Doraiswamy PC, Thompson DR (1982) A crop moisture stress index for large areas and its application in the prediction of spring wheat phenology. Agricultural Meteorology 27:1–15. https://doi.org/10.1016/0002-1571(82)90014-0
32. Ali AR, Ramadan MWA, Zometa P (2025) Machine learning for EMG-based gesture recognition in brain–computer interfaces and humanoid robots. Int J Intell Robot Appl 9:1789–1800. https://doi.org/10.1007/s41315-025-00463-1
33. Bhandari V, Huchaiah MD (2022) A new design of epileptic seizure detection using hybrid heuristic-based weighted feature selection and ensemble learning. Int J Intell Robot Appl 6:668–693. https://doi.org/10.1007/s41315-022-00233-3
34. Venkatasaichandrakanth P, Iyapparaja M (2024) A survey on pest detection and classification in field crops using artificial intelligence techniques. Int J Intell Robot Appl 8:709–734. https://doi.org/10.1007/s41315-024-00347-w
35. Wang Y, Yue X, Tian H, et al (2026) Mix-soil-spectra: Near-infrared spectroscopy combined with contrastive and ensemble learning for accurate prediction of soil organic matter and total nitrogen. Artificial Intelligence in Agriculture. https://doi.org/https://doi.org/10.1016/j.aiia.2026.04.011
36. Brereton RG, Lloyd GR (2014) Partial least squares discriminant analysis: taking the magic away. J Chemom 28:213–225. https://doi.org/https://doi.org/10.1002/cem.2609
37. De Maesschalck R, Candolfi A, Massart DL, Heuerding S (1999) Decision criteria for soft independent modelling of class analogy applied to near infrared data. Chemometrics and Intelligent Laboratory Systems 47:65–77. https://doi.org/https://doi.org/10.1016/S0169-7439(98)00159-2
38. Nagpal M, Gupta K, Gupta T, et al (2025) Advancing microplastic pollution management in aquatic environments through artificial intelligence. J Environ Health Sci Eng 23:33. https://doi.org/10.1007/s40201-025-00958-w
39. Kumar V, Aydav PSS, Minz S (2024) Crop Seeds Classification Using Traditional Machine Learning and Deep Learning Techniques: A Comprehensive Survey. SN Comput Sci 5:1031. https://doi.org/10.1007/s42979-024-03379-y
40. Cortes C, Vapnik V (1995) Support-vector networks. Mach Learn 20:273–297. https://doi.org/10.1007/BF00994018
41. Hnaien I Ben, Gascard E, Simeu-Abazi Z, et al (2025) Unsupervised anomaly detection in robotic systems via high-fidelity Digital Twins and deep autoencoders. Int J Intell Robot Appl. https://doi.org/10.1007/s41315-025-00509-4
42. Lv P, Zhang C, Yi F, et al (2024) A Novel FSVM with PSO for gait phase detection based on elastic pressure sensing insole system. Int J Intell Robot Appl 8:596–608. https://doi.org/10.1007/s41315-024-00334-1
43. Breiman L (2001) Random Forests. Mach Learn 45:5–32. https://doi.org/10.1023/A:1010933404324